
QCPINN: QUANTUM-CLASSICAL PHYSICS-INFORMED NEURAL NETWORKS FOR SOLVING PDES

Afrah Farea

Computational Science and Engineering Department, Informatics Institute
 Istanbul Technical University
 Istanbul 34469, Turkiye
 farea16@itu.edu.tr@email

Saiful Khan

Scientific Computing, Rutherford Appleton Laboratory
 Science and Technology Facilities Council (STFC)
 OX11 0QX, United Kingdom
 saiful.khan@stfc.ac.uk

Mustafa Serdar Celebi

Computational Science and Engineering Department, Informatics Institute
 Istanbul Technical University
 Istanbul 34469, Turkiye
 mscelebi@itu.edu.tr

ABSTRACT

Physics-informed neural networks (PINNs) have emerged as promising methods for solving partial differential equations (PDEs) by embedding physical laws within neural architectures. However, these classical approaches often require a large number of parameters to achieve reasonable accuracy, particularly for complex PDEs. In this paper, we present a quantum-classical physics-informed neural network (QCPINN) that combines quantum and classical components, allowing us to solve PDEs with significantly fewer parameters while maintaining comparable accuracy and convergence to classical PINNs. We systematically evaluated two quantum circuit architectures across various configurations on five benchmark PDEs to identify optimal QCPINN designs. Our results demonstrate that the QCPINN achieves stable convergence and comparable accuracy, while requiring approximately 10% of the trainable parameters used in classical approaches. It also results in a 40% reduction in the relative error L_2 for the convection-diffusion equation. These findings demonstrate the potential of parameter efficiency as a measurable quantum advantage in physics-informed machine learning, significantly reducing model complexity while preserving solution quality. This approach presents a promising solution to the computational challenges associated with solving PDEs.

1 Introduction

Recent advancements in machine learning have transformed approaches to solving PDEs, with PINNs emerging as an innovative technique. PINNs embed physical laws directly into neural network architectures, eliminating the need for labeled training data while strictly enforcing physical constraints. This approach has demonstrated considerable success in modeling various physical phenomena across scientific and engineering domains [1, 2, 3]. Although they hold great potential, research is underway to improve the accuracy of PINNs in modeling different PDEs and physical systems. They often face challenges with stiff systems, capturing steep gradients, and efficiently navigating high-dimensional parameter spaces. While increasing model expressivity through additional parameters can alleviate these challenges, this approach introduces new problems: increased computational cost, risk of overfitting, and unstable convergence

behavior during training [4, 5]. Such a trade-off between model complexity, generalization, and convergence ability is a fundamental challenge in neural network design.

Quantum computing presents a promising paradigm for overcoming these limitations. With its ability to process high-dimensional data and exploit quantum principles such as superposition and entanglement, quantum algorithms offer unique advantages for solving complex computational problems. For instance, the Harrow-Hassidim-Lloyd (HHL) algorithm has demonstrated theoretical exponential speedups for specific linear systems, while variational quantum algorithms provide practical near-term solutions [6, 7, 8]. Moreover, recent developments [9, 10, 11] indicate that quantum neural networks possess an expressive power that could significantly enhance the learning capabilities for modeling complex physical systems.

Although both PINNs and quantum computing have advanced independently, their integration remains largely unexplored. Several preliminary efforts have emerged: Sedykh et al. proposed HQPINN [12], focusing on computational fluid dynamics in 3D Y-shaped mixers; Dehaghani et al. introduced QPINN [13], integrating a dynamic quantum circuit with classical computing methodologies for optimal control problems; Trahan et al. [14] investigated both purely quantum and hybrid PINNs, highlighting parameter efficiency but limiting application to parametrized quantum circuit (PQC) networks with simple PDEs. Leong et al. proposed HQPINN [15], which is inspired by Fourier neural operators. However, existing research has not comprehensively established whether quantum-enhanced models can improve upon purely classical PINNs across a broad range of PDEs efficiently and reliably.

We aim to investigate the limitations of traditional PINNs by integrating quantum computing circuits with classical neural networks. We propose that such an integrated or hybrid approach can leverage complementary strengths: classical computing’s robustness and quantum computing’s enhanced expressivity and inherent parallelism. We believe this method will allow us to solve a wide range of PDEs with similar or better accuracy and convergence rates compared to classical PINNs, while requiring significantly fewer trainable parameters than classical models.

To this end, we introduce a hybrid architecture named Quantum-Classical Physics-Informed Neural Network (QCPINN). To search for a suitable QCPINN architecture and its configurations, we systematically evaluate multiple dimensions of the design space: two quantum circuit architectures: (a) discrete-variable (DV) qubit-based circuits with configurations, such as four circuit topologies: alternate, cascade, cross-mesh, and layered; and two embedding schemes: amplitude and angle; (b) continuous-variable (CV) circuits with configurations, including two measurement schemes: number and quadrature; three nonlinear operations: Kerr, cubic phase, and cross-Kerr; and two parameterizations: phase-free (magnitude) and full (magnitude and phase). We evaluate the performance of these QCPINN models across various PDEs, such as the Helmholtz and lid-driven cavity equations, while also extending our analysis to the Klein-Gordon, wave, and convection-diffusion equations. Our comprehensive assessment compares (a) solution accuracy, (b) convergence rates, and (c) parameter efficiency between classical PINNs and QCPINN variants.

To ensure reproducibility and facilitate broader adoption of our methods, we have made all components of QCPINN open-source code and publicly available on GitHub at <https://github.com/afrah/QCPINN>. We hope this repository will enable community engagement and collaborative advancement of this emerging field.

2 Background

2.1 Physics Informed Neural Network (PINNs)

PINNs [16] provide a framework to embed governing physical laws directly into neural network architectures. The PINN loss function combines terms representing governing equations and boundary conditions designed to minimize deviations from physical laws. More formally, the PINN loss function can be defined as:

$$\begin{aligned} \mathcal{L}(\theta) &= \arg \min_{\theta} \sum_{k=1}^n \lambda_k \mathcal{L}_k(\theta) \\ &= \arg \min_{\theta} \left(\lambda_1 \mathcal{L}_1(D[u_{\theta}(\mathbf{x}); \mathbf{a}] - f(\mathbf{x})) + \sum_{k=2}^n \lambda_k \mathcal{L}_k(B[u_{\theta}(\mathbf{x})] - g_k(\mathbf{x})) \right), \end{aligned} \quad (1)$$

where, n denotes the total number of loss terms, λ_k are the weighting coefficients, and θ represents trainable parameters. Here, $[D[u_{\theta}(\mathbf{x}); \mathbf{a}]$ and $[B[u_{\theta}(\mathbf{x})]$ are the arbitrary differential operators and initial/boundary conditions, respectively, that are applied to the output of the neural network $u_{\theta}(\mathbf{x})$. While the initial and boundary conditions ensure that the network output satisfies predefined constraints at specific spatial or temporal locations, the physics loss acts as a regularizer, guiding the network to learn physically consistent solutions and preventing overfitting to sparse or noisy

data. The balance between these loss components is crucial for achieving accurate solutions, as improper weighting can lead to underfitting the initial/boundary conditions or failing to capture the system dynamics correctly.

2.2 Continuous Variable (CV) QNN

In photonic quantum computing, CV computation addresses quantum states with continuous degrees of freedom, such as the position (x) and momentum (p) quadratures of the electromagnetic field. The computational space is, in principle, unbounded, involving infinite-dimensional Hilbert spaces with continuous spectra. To make these simulations computationally feasible, a cutoff dimension is employed to limit the number of basis states used for approximation. The computational state space is defined as $r = n^m$, where m represents the number of qumodes and n is the cutoff dimension. For example, with three qumodes and a cutoff dimension of 2, the state space is 8-dimensional. Ideally, higher cutoff dimensions (up to a certain threshold) yield more precise results but at the cost of increased computational complexity.

In this work, we adhere to the affine transformation introduced in [17]. The proposed circuit ansatz consists of a sequence of operations that manipulate quantum states in the phase space. Each layer of the CV-circuit QNN includes the following key components:

1. **Interferometers** ($U_1(\psi_1, \phi_1)$ and $U_2(\psi_2, \phi_2)$): Linear optical interferometers perform orthogonal transformations, represented by symplectic matrices. These transformations adjust the state by applying rotation and mixing between modes, corresponding to beam splitting and phase-shifting operations.
2. **Squeezing Gates** ($S(r, \phi_s)$): These gates scale the position and momentum quadratures independently, introducing anisotropic adjustments to the phase space. Encoding sharp gradients using squeezing gates is particularly appealing for PDE solvers, as it allows fine-tuning of local characteristics [12].
3. **Displacement Gates** ($D(\alpha, \phi_d)$): These gates shift the state in phase space by adding a displacement vector α , translating the state globally without altering its internal symplectic structure.
4. **Non-Gaussian Gate** ($\Phi(\lambda)$): To introduce nonlinearity, a non-Gaussian operation, such as a cubic phase, Kerr, and cross-Kerr gates, is applied. This step enables the neural network to approximate nonlinear functions and enhances the ability to solve complex, nontrivial PDEs.

These components together mimic the classical affine transformation such that:

$$L(|x\rangle) = |\Phi(Mx + b)\rangle = \Phi(D \circ U_2 \circ S \circ U_1), \quad (2)$$

where, M represents the combined symplectic matrix of the interferometers and squeezing gates, x is the input vector in the phase space, b is the displacement vector, and Φ is the nonlinear transformation.

In addition to the building blocks above, CV-circuit QNNs offer flexibility in measurement schemes and parameterization strategies. Measurement can be performed in either the number basis, which projects the state onto discrete photon-number states, or the quadrature basis, which yields continuous-valued outcomes corresponding to position or momentum observables. Furthermore, the parameterization of unitary operations may be either full (including both magnitude and phase) or restricted to magnitude-only (by setting phase parameters ϕ to zero), which can improve trainability and mitigate optimization challenges at the cost of reduced expressivity.

Although such a model exhibits intriguing theoretical properties, their practical implementation in real-world problem solving seems to suffer from fundamental stability issues. This is mainly due to their inherent sensitivity and reliance on continuous degrees of freedom, which complicate optimization compared to DV-based approaches (discussed in detail in section 2.3). This sensitivity stems from several factors, including the precision required for state preparation, noise from decoherence, and the accumulation of errors in variational quantum circuits. Furthermore, the transformations involved in CV quantum circuits are prone to numerical instabilities, particularly when optimized using gradient-based methods, as seen in the following section. Although foundational studies about the barren plateau problem, such as [18, 19, 20], primarily address DV circuit systems, the analysis indicates that similar issues can arise in CV quantum systems. In particular, the infinite-dimensional Hilbert space and the continuous nature of parameterization can exacerbate barren-plateau effects.

2.3 Discrete Variable (DV) QNN

DV-circuit quantum models do not inherently provide affine transformations as a core feature like CV-based QNNs. However, they can achieve affine-like behaviour through parameterized single-qubit rotations, controlled operations, and phase shifts for amplitude adjustments. Therefore, the affine transform of equation (2) can be reinterpreted to align with their architecture such that:

1. **Mx + b:** can be achieved through a combination of parameterized quantum gates:
 - U_1, U_2 : A unitary operator that can be represented by parameterized single-qubit rotations, such as $R_x(\theta), R_y(\theta)$, or $R_z(\theta)$.
 - S : A sequence of controlled gates (e.g., CNOT and CZ) responsible for introducing entanglement, which enables the representation of correlated variables and interactions.
 - D : Data encoding circuits that map classical data into quantum states through techniques such as basis embedding, amplitude embedding, or angle embedding.
2. **Non-linear Activation (Φ):** DV-circuit QNNs lack intrinsic quantum nonlinearity due to the linearity of quantum mechanics. However, classical measurements or a combination of classical measurements and non-linear activation functions (such as *Tanh*) can be applied to the output between quantum layers [21, 22].

3 Related Work

In the domain of PDE solvers, quantum algorithms can be broadly categorized into two primary approaches: (a) exclusively quantum algorithms and (b) hybrid quantum-classical methods.

3.1 Exclusively Quantum Algorithms

Exclusively quantum algorithms for solving PDEs typically leverage unitary operations and quantum state embedding techniques to achieve a computational advantage. In contrast to neural networks, exclusively quantum algorithms use fixed quantum circuit structures with no trainable parameters. The celebrated Harrow-Hassidim-Lloyd (HHL) algorithm is an example of this category, which provides exponential speedups to solve linear systems under specific conditions [23]. Extensions of the HHL algorithm have been applied to solve sparse linear systems derived from discretized linear [24, 25] or nonlinear [26] PDEs, leveraging numerical techniques such as linear multistep method [27], Chebyshev pseudospectral method [28], and Taylor series approximations [29]. In fluid dynamics applications, lattice-gas quantum models have been examined for directly solving PDEs [30, 31] or PDEs derived from ODEs through methods such as the Quantum Amplitude Estimation Algorithm (QAEA) [32, 33].

Despite these advancements, purely quantum algorithms for solving PDEs encounter practical challenges such as requirements for quantum error correction [34, 35, 36], limitations in circuit depth [37, 31, 38], and bottlenecks in data embedding [39, 40, 41]. These obstacles, among others, limit the near-term viability of exclusively quantum PDE solvers on today’s noisy intermediate-scale quantum (NISQ) devices.

3.2 Hybrid Quantum-Classical Approaches

Hybrid quantum-classical approaches have emerged as promising solutions to overcome the limitations of exclusively quantum algorithms. These methods combine the robustness, maturity, and stability of classical computation with the enhanced capacity, expressivity, and inherent parallelism of quantum systems. While classical components can efficiently handle pre-/post-processing, optimization, and error stabilization, quantum layers can capture intricate patterns, solve sub-problems, and accelerate specialized computations.

Within this hybrid paradigm, Quantum Neural Networks (QNNs) have demonstrated universal approximation capabilities for continuous functions when implemented with sufficient depth, width, and well-designed quantum feature maps [42, 43, 44]. For instance, Salinas et al. [45] showed that single-qubit networks with iterative input reuploading can approximate bounded complex functions, while Goto et al. [46] established universal approximation theorems for quantum feedforward networks. Schuld et al. [9] revealed that the outputs of parameterized quantum circuits (with suitable data embedding and circuit depth) can be expressed as truncated Fourier series, thereby providing theoretical support for the universal approximation ability of QNNs. Liu et al. [47] provided formal evidence of quantum advantage in function approximation. These developments not only support applications in solving PDEs and optimization tasks but also extend to other computational tasks such as quantum chemistry [48], material sciences [49, 50], and pattern recognition [51], to name a few.

A well-known example of this integrated approach is the Variational Quantum Algorithms (VQA), also known as Variational Quantum Circuits (VQC). These algorithms employ parameterized quantum circuits with tunable gates optimized through classical feedback loops. VQA implementations for solving PDEs include the Variational Quantum Eigensolver (VQE)[52, 53], Variational Quantum Linear Solver (VQLS)[54], and Quantum Approximate Optimization Algorithm (QAOA)[55], as well as emerging methods like Differentiable Quantum Circuits (DQCs)[56, 57], quantum kernel methods [58], and Quantum Nonlinear Processing Algorithms (QNPA) [59].

Table 1: This work examines different configurations of the QCPINN along with the list of PDEs used for testing and generalization.

QNN	Configurations		PDEs	
	Type	Options	Testing	Generalization
CV-circuit	Measurement scheme	Number, quadrature		
	Nonlinear operations	Kerr, cubic phase, cross-kerr		
	Parameterization	Phase-free (magnitude), Full (magnitude and phase) (also refer to algorithm 1)	Helmholtz, Lid-driven cavity	Wave, Klein-Gordon, Convection-diffusion
DV-circuit	Embeddings	Amplitude, angle		
	Topology	Alternate, cascade, cross-mesh, layered (also refer to Fig. 2 and table 2)		

The aforementioned methods primarily utilize qubit-based quantum computing, which represents the predominant paradigm in quantum computing literature. However, continuous-variable quantum computing (CVQC) [60] offers an alternative computational model that leverages continuous degrees of freedom, such as quadratures and electromagnetic field momentum as discussed in section 2.2. For instance, in [61], Gaussian and non-Gaussian gates were used to manage continuous degrees of freedom, offering enhanced scalability and expressivity for continuous systems. For consistency, we refer to qubit-based models as discrete-variable (DV) circuit models throughout this paper.

Recently, VQA methods have been extended to Physics-informed quantum neural networks (PIQNN) [62, 13, 14, 12, 15], broadening their applicability across physics and engineering domains. These hybrid methods offer several distinct advantages when implemented within the PINN framework.

Firstly, these models enable the flexible configuration of inputs and outputs independent of qubit/qumode counts or quantum layer depth, making them particularly effective for scenarios where the input dimension (e.g., temporal and spatial coordinates) differs from output dimensions (e.g., dependent variables like velocity, pressure, and force).

Secondly, hybrid approaches facilitate increased trainable parameter counts without the need for deeper quantum circuits, additional qubits, or higher cutoff dimensions in CV quantum systems. These factors are particularly crucial in the NISQ era, where hardware constraints impose strict limits on circuit depth and coherence times, making deeper quantum networks computationally expensive and impractical [63, 64].

Thirdly, these qualities are especially advantageous for PINNs, where shallow network architectures are favored to optimize the balance between computational efficiency and solution accuracy [65, 66, 67, 5].

Finally, a substantial benefit of such hybrid models is the integration of automatic differentiation within both classical and quantum networks. This capability, supported by contemporary software packages like PennyLane [68] and TensorFlow Quantum [69], enables the automatic computation of derivatives as variables are directly incorporated into the computational graph. This approach simplifies PINN implementation and facilitates the efficient handling of complex physics-informed loss functions and higher-order derivatives.

Our work is related to the approaches in [12, 13, 14, 15], but with several key differences. While HQPINN [12] focuses specifically on computational fluid dynamics in 3D Y-shaped mixers using a fixed quantum depth with an infused layer structure, the QPINN [13] integrates a dynamic quantum circuit combining Gaussian and non-Gaussian gates with classical computing methodologies within a PINN framework to solve optimal control problems. In addition, the model proposed in [14] investigates both purely quantum and hybrid PINNs, highlighting parameter efficiency but relying on limited PQC networks and addressing primarily simple PDEs. Recently proposed HQPINN [15], inspired by Fourier neural operator (FNO) [70], introduces a parallel hybrid architecture to separately model harmonic and non-harmonic features before combining them for output.

4 Quantum-Classical Physics-Informed Neural Networks (QCPINN)

Fig. 1 illustrates a high-level overview of our proposed QCPINN. The preprocessor consists of a two-layer neural network architecture, ensuring that the overall framework is sufficiently shallow for efficient training while also being deep enough to capture essential transformations. Each layer is composed of 50 neurons. The first layer performs a linear transformation to modify the input dimension, followed by a *Tanh* activation function to introduce non-linearity. The second layer subsequently maps the transformed inputs to the QNN layer (or classical NN layer used for comparison).

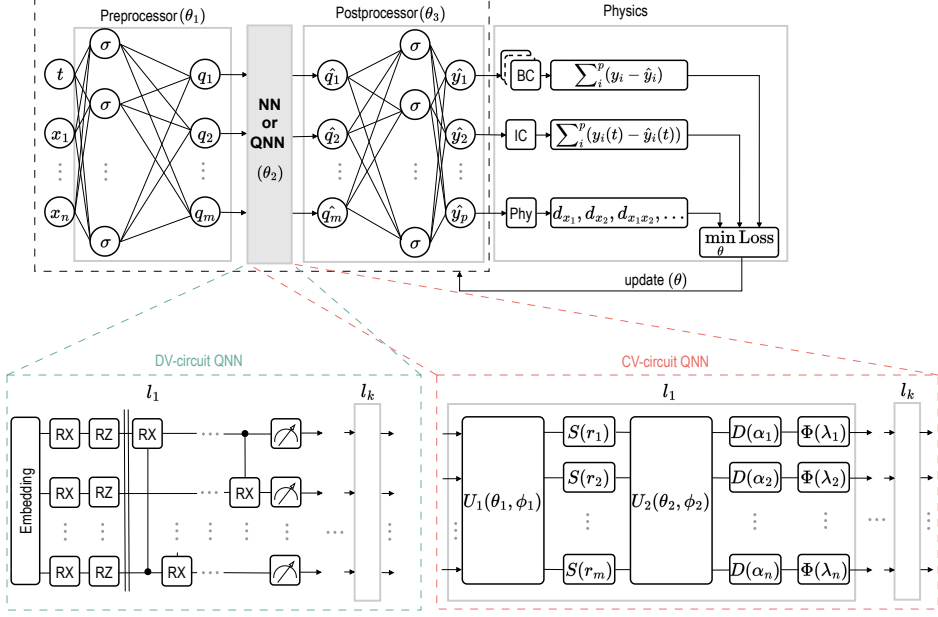


Figure 1: Architecture of the quantum-classical physics-informed neural network (QCPINN) framework. The figure illustrates the hybrid structure: a classical preprocessor encodes the inputs, which are then fed into the QNN or classical neural network (NN). The QNN is implemented as either a CV-circuit or a DV-circuit with k layers. A classical postprocessor then decodes the QNN or NN outputs. The integrated loss function concurrently minimizes PDE residuals and initial/boundary condition errors, ensuring the model adheres to physical constraints throughout training. Table 1 lists the various configurations of the CV and DV-circuits studied in this work.

Likewise, the postprocessor layer replicates the preprocessor structure with appropriate dimensions, ensuring a symmetric transformation between classical and quantum representations. This design offers flexibility in managing quantum feature representations while ensuring the higher-order differentiability required for residual loss in the proposed QCPINN model.

4.1 CV-circuit QCPINN

The CV-circuit QCPINN consists of three primary components: a preprocessor network, a CV-circuit quantum network (the QNN layer of Fig. 1), and a postprocessor network. The quantum network is adapted from [17] and is described in algorithm 1. Each layer of the quantum network executes a sequence of quantum operations.

Table 1 presents various configurations of our CV-circuit studied to identify a suitable parameterization scheme, nonlinear operation, and measurement approach. For measurement schemes, we evaluated both number and quadrature. For parameterization, we examined phase-free using only magnitude parameters and full parameterization using both magnitude and phase parameters. For nonlinear operations, we explored Kerr nonlinearity, cubic phase gates, and cross-Kerr interactions. Additionally, the quantum state is measured, typically in either the quadrature basis $\langle \hat{q}_i \rangle$ or the Fock number basis $\langle \hat{n}_i \rangle$, to yield classical outputs for the postprocessing layers. Please refer to section 2.2 for additional details.

Structuring the network as described in algorithm 1 results in a circuit depth of $(2n + 3)L$, while the number of trainable quantum parameters increases to $\mathcal{O}(n^2 L)$, where n represents the number of qumodes and L denotes the number of layers.

4.2 DV-circuit QCPINN

The DV-circuit QCPINN consists of three primary components: a preprocessor network, a DV-circuit quantum network (the QNN layer of Fig. 1), and a postprocessor network. The quantum network is a custom DV-circuit, which executes quantum operations on the preprocessed data.

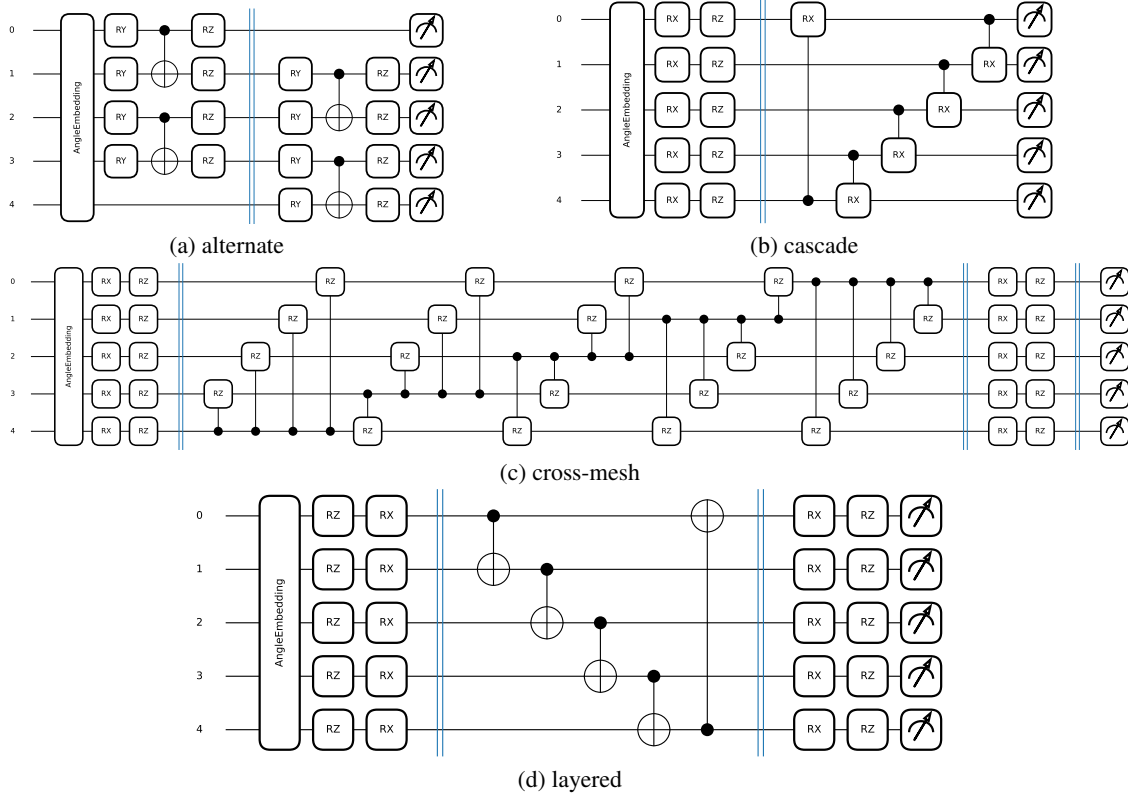


Figure 2: DV-circuit topologies evaluated in this study, shown with five qubits and angle embedding as an example. Square boxes denote parameterized single-qubit rotation gates, and lines with dots indicate entangling operations (e.g., CNOT gates). The characteristics of these circuits are shown in table 2.

Table 2: Characteristics of the topologies used in DV-circuits in Fig. 2. n is the number of qubits, and L is the number of layers.

Topology	Circuit Depth	Circuit Connectivity	Number of Parameters	Number of two-qubit gates
alternate	$6L$	Nearest-neighbor	$4(n-1)L$	$(n-1)L$
cascade	$(n+2)L$	Ring topology	$3nL$	nL
cross-mesh	$(n^2 - n + 4)L$	All-to-all	$(n^2 + 3n)L$	$(n^2 - n)L$
layered	$6L$	Nearest-neighbor	$4(n-1)L$	$(n-1)L$

Table 1 presents various configurations of our DV-circuit studied to identify a suitable embedding scheme and topology. Fig. 2 illustrates four proposed ansätze named after their topology: alternate, cascade, cross-mesh, and layered. These circuits are adapted from literature, including [71, 72, 73, 62]. Table 2 presents features of the DV-circuits across the key descriptors, circuit depth, connectivity, number of parameters, and the number of two-qubit gates. These circuits agree with the affine transformation discussed in section 2 and adhere to the hardware-efficient ansatz (HEA) [74] defined as:

$$U(\psi) = \prod_k U_k(\psi_k) W_k, \quad (3)$$

where, each layer k alternates between single-qubit parameterized rotations, $U_k(\psi_k)$, and an entangling operation, W_k .

The **cross-mesh** ansatz implements an all-to-all connectivity scheme, facilitating extensive interaction between qubits, which enhances its ability to explore the Hilbert space. The circuit depth scales as $\mathcal{O}(n^2 - n + 4)L$, while the number of trainable parameters is $(n^2 + 3n)L$. The use of global entanglement fosters strong correlations between qubits; however, it results in greater circuit depth, resource demands, and training difficulties [20]. This circuit's total number of two-qubit gates is also significantly higher than in other ansätze.

Algorithm 1 CV-circuit QNN

Require: Qumodes: num_qumodes, Layers: num_layers, Device: d , Cutoff: c , Input: Tensor x
Ensure: Output: Tensor y

- 1: **Initialize Parameters:**
- 2: $\psi_1, \psi_2, \phi_1, \phi_2, \phi_s, \phi_d \sim \mathcal{N}(0, 0.01\pi)$ (interferometer), $\alpha, r \sim \mathcal{N}(0, 0.001)$, $\Phi \sim \mathcal{N}(0, 0.001)$ (nonlinearity)
- 3: **Quantum Device:** Initialize d with num_qumodes, cutoff c .
- 4: **procedure** QUANTUMCIRCUIT(input)
- 5: **for** $i = 1$ to num_qumodes **do**
- 6: Encode Inputs with Displacements D : $D(\text{input}[i], 0)$ ▷ only real amplitudes
- 7: **end for**
- 8: **for** $l = 1$ to num_layers **do**
- 9: Apply Interferometer($\psi_1[l], \phi_1[l]$) ▷ Phase-free: $\phi_s[l] = 0.0$
- 10: Apply Squeezing($r[l], \phi_s[l]$) ▷ Phase-free: $\phi_d[l] = 0.0$
- 11: Apply Interferometer($\psi_2[l], \phi_2[l]$) ▷ Phase-free: $\phi_d[l] = 0.0$
- 12: Apply Displacement($\alpha[l], \phi_d[l]$) ▷ Options: Kerr, Cubic Phase, Cross-Kerr
- 13: Apply Nonlinearity Φ
- 14: **end for**
- 15: Measure state for each wire ▷ Measurement options: $\langle \hat{q}_i \rangle$ (Quadrature) or $\langle \hat{n}_i \rangle$ (Number)
- 16: **return** Measurements
- 17: **end procedure**
- 18: **procedure** INTERFEROMETER($\psi, \phi_{\text{bs}}[l]$)
- 19: **for** $l = 1$ to num_qumodes **do**
- 20: **for** (q_1, q_2) in Pairs(num_qumodes) **do**
- 21: **if** $(l + k)\%2 \neq 1$ **then**
- 22: Apply Beamsplitter $B(\psi[n], \phi_{\text{bs}}[n])$ ▷ Phase-free: $\phi_{\text{bs}}[n] = 0.0$
- 23: **end if**
- 24: **end for**
- 25: **end for**
- 26: **for** $i = 1$ to num_qumodes $- 1$ **do**
- 27: Apply Rotation $R_Z(\psi[i])$
- 28: **end for**
- 29: **end procedure**
- 30: **procedure** FORWARDPASS(Input x)
- 31: $y \leftarrow \text{QuantumCircuit}(x)$
- 32: **return** y
- 33: **end procedure**

The **cascade** ansatz balances expressivity and hardware efficiency by employing a ring topology for qubit connectivity. This design facilitates efficient entanglement while keeping the circuit depth manageable at $(n + 2)L$. The circuit contains $3nL$ trainable parameters, making it more efficient than cross-mesh while maintaining reasonable expressivity. Incorporating controlled rotation gates (CR_X) improves entanglement compared to CNOT gates and increases the circuit's capacity to explore the Hilbert space. Furthermore, the requirement for two-qubit gates is fewer than that of cross-mesh, thus lowering the overall computational cost.

The **layered** ansatz features a structured design that includes alternating rotation and entangling layers. Each qubit undergoes parameterized single-qubit rotations, typically utilizing R_X and R_Z gates. Entanglement is achieved through nearest-neighbor CNOT gates, ensuring compatibility with hardware constraints while maintaining efficient connectivity. Compared to the cross-mesh's all-to-all connectivity or the cascade's ring topology, the layered architecture represents a compromise between expressivity and hardware efficiency.

The **alternate** ansatz uses an alternating-layer structure featuring nearest-neighbor CNOT gates, ensuring effective entanglement while maintaining a manageable circuit depth of $6L$. The total number of trainable parameters in this circuit $4(n - 1)L$ aligns with the layered ansatz. The entanglement structure determined by the alternating CNOT layers offers the highest level of entangling capability among the circuits studied. Consequently, the cross-mesh ansatz provides the largest parameter count and highest expressivity, whereas the alternate circuit excels in entangling capabilities.

Compared to the QNN models discussed above, we can see that the classical feed-forward neural networks (NNs) exhibit a more flexible scaling pattern, with trainable parameters $\mathcal{O}(h^2L)$, where h denotes the number of hidden neurons (assuming a fixed width h in all hidden layers) with independent selection of h . Therefore, while classical models depend on deep architectures and larger parameter counts, quantum networks achieve expressivity by utilizing intrinsic quantum correlations and exponential scaling of the Hilbert space.

5 Implementation and Training Details

We used PyTorch’s automatic differentiation to compute the gradients for both classical and quantum parameters. The training was carried out with a batch size of 64 and a maximum of 20,000 epochs in all case studies, except in the cavity problem, where we used 12,500 maximum iterations. The Adam optimizer was used to ensure stable convergence. These settings were uniformly applied across all study cases to provide a consistent basis for comparison. For the cavity problem, initial training data was selected using the Sobol sequence, and then random sampling with a batch size of 128 was applied to this Sobol-generated dataset during training. For all other cases, only random sampling with a batch size of 128 was used throughout the entire process.

While other training configurations, such as increasing the number of iterations or adjusting the batch size, could yield better performance, the goal is to evaluate the models under identical conditions. Given the near-infinite hyperparameter space, this controlled evaluation ensures a fair assessment of the relative strengths and limitations of each approach. It is also important to acknowledge that the quantum experiments conducted in this study were performed using emulator-based simulations rather than actual quantum hardware. These simulations inherently operate at significantly reduced speeds compared to their classical counterparts due to the substantial computational overhead associated with emulating quantum circuits on classical machines. Future implementations on actual quantum hardware would eliminate this simulation overhead, potentially revealing additional performance characteristics not captured in the current study.

In our initial implementation, we observed that the experiments on the CPU were faster than those on the GPU. This is likely due to our study’s relatively small batch size, circuit complexity, and limited number of qubits/qumodes: five qubits for DV-circuit models and two qumodes for CV-based models. Moreover, the quantum backends employed in our experiments are not optimized for GPU efficiency. Considering these limitations, we have chosen to conduct our experiments on a CPU system with 6148 CPUs (each operating at 2.40 GHz) and 192 GB of RAM. Further details on training configurations and implementation strategies are provided in the following subsections.

5.1 CV-circuit QCPINN

We used the PennyLane framework [68] with the Strawberry Fields Fock backend [75] to develop and train our CV-circuit QCPINN model. Each CV-circuit layer was configured for two qumodes with a cutoff dimension of 20. Quantum parameters were initialized using controlled random distributions, with small values for active parameters (e.g., r , d) to ensure numerical stability. Classical PINN’s layers were initialized using Xavier initialization. During training, either position quadrature (X) or number operator expectation measurements are performed on each qumode to extract continuous-valued features from the quantum state.

The CV-circuit operations are carefully managed to ensure numerical stability. For instance, squeezing operations are highly sensitive to large values, as excessive squeezing amplifies quadrature fluctuations, which increases photon number variance and truncation errors in Fock-space representations [76]. Similarly, displacement operations are constrained to prevent quantum states from exceeding computational cutoffs, as this can introduce simulation errors [77]. Likewise, the nonlinear operations such as Kerr gate can cause phase shifts that scale quadratically with photon numbers, making them highly sensitive to large values [78].

Therefore, we used a learning rate of 1.0×10^{-4} to address the model’s sensitivity to gradient updates. A ReduceLROnPlateau scheduler was implemented with a patience of 20 epochs, decreasing the learning rate by a factor of 0.5 when no improvement was observed, down to a minimum of 1.0×10^{-6} . Additionally, we applied gradient clipping to prevent exploding gradients, restricting their norm to a maximum of 0.1. As shown in algorithm 1, we also scaled the training parameters by small factors to further stabilize the CV transformations.

While these settings can alleviate the instability and prevent divergence in quantum state evolution, they can also introduce the vanishing gradient problem. This issue is well-documented in classical neural network literature and occurs when excessively small initialization values diminish gradients during backpropagation, slowing or even halting the learning process [79].

5.2 DV-circuit QCPINN

We used Adam optimizer with a learning rate of 0.005 to train the DV-circuit QCPINN. A learning rate scheduler, ReduceLROnPlateau, is employed to adjust the learning rate when the loss plateaus dynamically. Specifically, the scheduler reduces the learning rate by a factor of 0.9 if no improvement is observed for 1000 consecutive epochs, promoting stability and convergence. Furthermore, the training function applies gradient clipping to prevent exploding gradients, clipping them according to their norm to ensure they do not exceed a unity value. During training, Pauli-Z expectation measurements are performed on each qubit to extract features from the quantum state.

Table 3: The CV-circuit QCPINN models the performance in solving the Helmholtz and lid-driven cavity equations. There are 12 combinations in total, as in Table 1. Among these results of the model with a quadrature measurement scheme, a Kerr nonlinear function, and phase-free parameterization is reported here. The remaining 11 combinations are not mentioned as the results are more or less similar. Training convergence is shown in Fig. 3.

PDE	# Parameters	Relative L_2 error (%)		Final loss
Helmholtz	469	u	1.00e + 02	5077.79
		f	1.00e + 02	
cavity	621	u	9.345e + 01	0.102
		v	9.979e + 01	
		p	8.620e + 01	

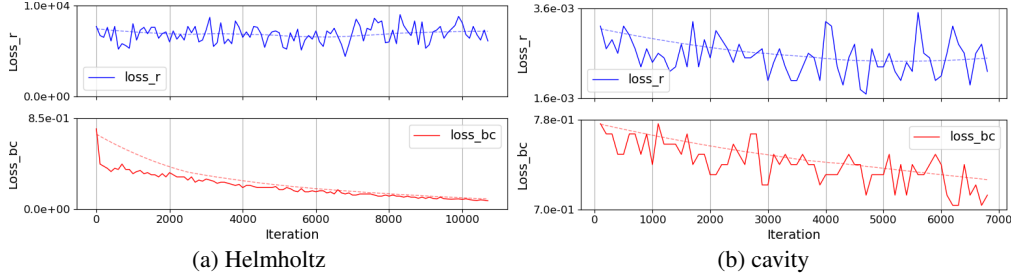


Figure 3: The training convergence behavior of the CV-circuit QCPINN model when solving (a) Helmholtz and (b) lid-driven cavity. The terms “loss_r” and “loss_{bc}” refer to residual and boundary losses. The “loss_{bc}” shows a decreasing trend, indicating improvements in satisfying the boundary conditions; however, the overall decrease is below expectation. The “loss_r” exhibits significant fluctuations and does not display a noticeable reduction, suggesting difficulties in minimizing the residual error of the governing equation.

5.3 Classical PINN Model

The classical baseline model consists of three main components: a preprocessing network, a neural network NN, and a postprocessing network (as shown in figure 1). The NN differs between two configurations: (a) In model-1, it includes two fully connected layers, each containing 50 neurons with a Tanh activation function between layers, and (b) In model-2, the NN is entirely omitted, meaning only the preprocessing and postprocessing networks are kept, simplifying the model’s structure.

These two models represent different levels of complexity, with model-1 having more layers and, consequently, a higher number of trainable parameters than model-2. We use these classical models to evaluate and compare the performance of the proposed hybrid models in figure 1. Training settings, including the optimizer and batch size, were kept consistent with the QCPINN models to allow for a fair comparison between classical and quantum-enhanced approaches. The learning rate is 0.005.

5.4 PDEs

We implemented five distinct PDEs, which include the Helmholtz, the time-dependent 2D lid-driven cavity, the 1D wave, the Klein-Gordon, and a convection-diffusion problems. The mathematical formulation, boundary conditions, and corresponding loss function designs for each PDE are detailed in A.

6 Results

We began testing our CV and DV-circuit QCPINN using two benchmark problems: Helmholtz and the lid-driven cavity.

6.1 CV-circuit QCPINN

At the beginning of our study, we implemented CV-circuit QCPINN models using 12 different combinations. This included two measurement schemes, three nonlinear functions, and two parameterization schemes (see Table 1). The results indicate that the behavior of these models is quite similar. Table 3 and Fig. 3 present the results and training convergence for the model that employs the quadrature measurement scheme, Kerr nonlinear function, and phase-free parameterization.

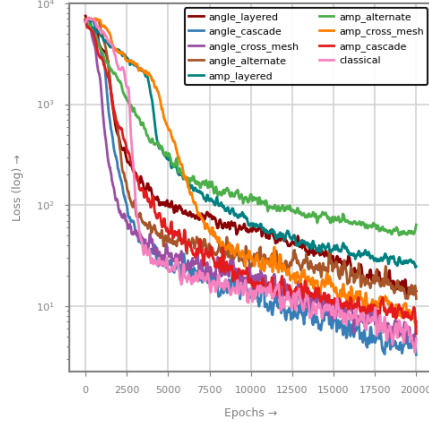


Figure 4: Training convergence history of our DV-based QCPINN models compared to best classical PINN model when solving the Helmholtz equation. The plots track the performance over 20,000 epochs, showing how QCPINN performs with two different embedding methods across four circuit topologies. For comparison, we include the classical PINN model-2, which outperforms model-1 in this case.

6.1.1 Helmholtz Equation.

For the Helmholtz Eq. 4, we used 469 trainable parameters. The results, in Table 3, show a high relative L_2 error for both the u and f variables, along with a significant final loss. The training convergence pattern in Fig. 3(a) highlights some challenges. For example, the boundary loss, “loss_bc”, shows a steady decrease over 10,000 iterations, suggesting that the model is gradually improving in meeting the boundary conditions. However, the residual loss, “loss_r”, remains consistently high, with substantial fluctuations throughout the training process. This indicates that the model was struggling to satisfy the differential equation itself.

6.1.2 Time-dependent 2D Lid-driven Cavity Equation.

For the more complex lid-driven cavity Eq. 5, the CV-circuit QCPINN model was implemented with 621 trainable parameters. The result, in Table 3, shows that the relative L_2 errors for both velocity and pressure variables remain high. However, the final loss value of 0.102 is significantly lower than that observed for the Helmholtz equation. Fig. 3(b) shows the training convergence, where the boundary loss exhibits some improvement, although it still experiences considerable fluctuations. The residual loss displays even greater oscillations compared to the Helmholtz case, indicating a greater challenge in accurately capturing the complex fluid dynamics governed by the Navier-Stokes equations.

This behavior is primarily attributed to gradient decay issues intrinsic to our CV-circuit implementation. The vanishing gradient problem [79] manifests more severely due to the additional constraints imposed by quantum operations. Small initialization values, while necessary to prevent divergence in quantum state evolution, significantly diminish gradients during backpropagation.

We examined various techniques, such as Xavier initialization for learnable parameters, gradient clipping, and skip connections, to mitigate the problem of gradient decay, but these attempts proved ineffective. Exploring alternative optimization strategies beyond standard gradient descent may be beneficial in addressing this issue, though this remains beyond the scope of this work.

6.2 DV-circuit QCPINN

The DV-circuit QCPINNs demonstrate stable performance compared to the CV-circuit across all the PDEs considered in this study. Thus, we perform a detailed analysis of the DV-circuit implementation throughout the remainder of this paper.

Our investigation began by using various DV-circuit configurations to solve two fundamental PDEs: Helmholtz and the lid-driven cavity. We systematically evaluated the performance across combinations of two distinct embedding approaches and four different circuit topologies, comparing these quantum implementations against classical models.

Table 4: Comparison of the performance of our DV-circuit QCPINN models against classical PINN approaches in solving the Helmholtz equation. The comparison metrics include the number of trainable parameters required by each model, the relative L_2 error in %, and the final training loss value achieved. u and f are the PDE solution and the force term.

	Embedding	Topology	# Parameters	Relative L_2 error (%) Final loss	
DV-circuit	amplitude	alternate	781	u f	$2.14e+01$ $1.21e+01$ 55.360
		cascade	771	u f	$1.99e+01$ $4.97e+00$ 6.372
		cross-mesh	836	u f	$1.77e+01$ $3.76e+00$ 6.872
		layered	781	u f	$4.05e+01$ $7.54e+00$ 39.441
	angle	alternate	781	u f	$9.15e+00$ $4.15e+00$ 11.456
		cascade	771	u f	$4.12e+00$ $1.64e+00$ 3.301
		cross-mesh	836	u f	$1.18e+01$ $3.76e+00$ 5.822
		layered	781	u f	$2.35e+01$ $5.73e+00$ 11.512
	Classical PINN	model-1	7851	u f	$3.18e+01$ $6.40e+00$ 20.331
		model-2	2751	u f	$6.72e+00$ $2.83e+00$ 4.771

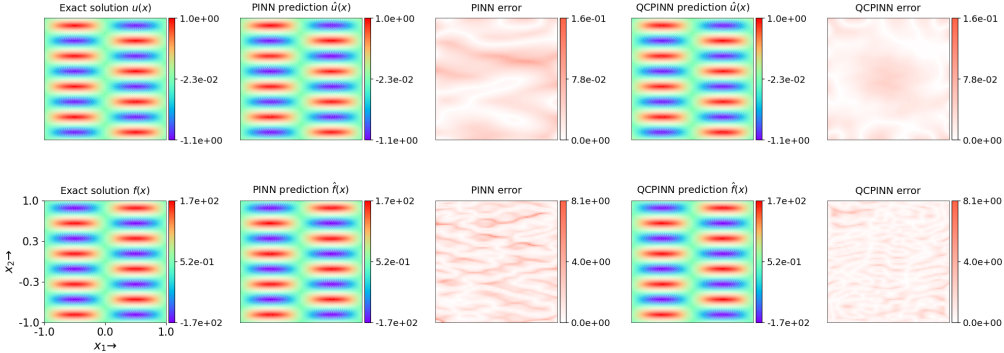


Figure 5: Comparison of the exact solution and the model predictions for the Helmholtz equation: the best classical PINN results (model-2), and our DV-circuit QCPINN using angle embedding (which outperforms amplitude embedding) with cascade topology (which outperforms the other three topologies). The first row shows the PDE solution u , while the second row shows the force field (f).

6.2.1 Helmholtz Equation.

Table 4 presents the performance of the DV-circuit QCPINN models in solving the Helmholtz Eq. 4 and comparing the results with classical models. The results show that the cascade topology consistently outperformed other topologies, achieving the lowest final training loss and low relative L_2 testing errors. In contrast, the layered and alternate circuit topologies show higher final training losses, especially the layered topology with amplitude embedding.

Fig. 4 compares the training loss convergence of DV-circuit QCPINN models to the classical PINN. The results indicate that DV-based quantum models display controlled convergence with relatively stable training dynamics. Moreover, the angle embedded cascade topology demonstrates the most competitive performance, achieving a loss level close to the best classical model while utilizing approximately 72% fewer parameters.

Fig. 5 visualizes the exact and predicted solutions for the Helmholtz equation. It also shows the prediction errors of both the best classical model and the angle-cascade QCPINN. While the classical model captures the overall structure, it exhibits noticeable discrepancies, as shown in the absolute error maps, which reveal significant deviations near the boundaries and at regions of sharp local gradients. In contrast, the predictions from the angle-cascade QCPINN model closely align with the exact solutions while using fewer parameters than the classical approach.

Table 5: Comparison of the performance of our DV-circuit QCPINN models against classical PINN approaches in solving the lid-driven cavity equation. The comparison metrics include the number of trainable parameters required by each model, the relative L_2 error in %, and the final training loss value achieved. u , v , and p are the velocity components and the pressure values, respectively.

Embedding	Topology	# Parameters	Relative L_2 error (%) Final loss		
DV	amplitude	933	u	$6.441e + 01$	
			v	$8.439e + 01$	0.127
			p	$6.102e + 01$	
	cascade	928	u	$6.670e + 01$	
			v	$8.409e + 01$	0.123
			p	$6.365e + 01$	
	cross-mesh	988	u	$7.073e + 01$	
			v	$4.893e + 01$	0.109
			p	$7.096e + 01$	
	layered	933	u	$5.690e + 01$	
			v	$9.476e + 01$	0.121
			p	$7.469e + 01$	
angle	alternate	933	u	$4.041e + 01$	
			v	$4.683e + 01$	0.109
			p	$4.746e + 01$	
	cascade	928	u	$2.745e + 01$	
			v	$2.081e + 01$	0.083
			p	$4.791e + 01$	
	cross-mesh	988	u	$2.035e + 01$	
			v	$2.071e + 01$	0.084
			p	$4.011e + 01$	
	layered	933	u	$4.572e + 01$	
			v	$6.628e + 01$	0.129
			p	$7.885e + 01$	
Classical PINN	model-1	8003	u	$2.103e + 01$	
			v	$3.027e + 01$	0.087
			p	$2.317e + 01$	
	model-2	2903	u	$3.830e + 01$	
			v	$2.924e + 01$	0.073
			p	$4.106e + 01$	

6.2.2 Time-dependent 2D Lid-driven Cavity Equation.

Table 5 presents the performance of the QCPINN methods for solving the lid-driven cavity Eq. 5. Among the DV-circuit QCPINN models, cascade achieves the best overall performance, demonstrating good convergence properties with the lowest final training loss. The models with angle embedding and cross-mesh topology also perform well, achieving the lowest final training loss and highlighting their effectiveness in this setting. Specifically, the angle-cascade quantum model achieves comparable performance to the best classical model while requiring only 12% of the parameters.

Fig. 6 compares the training loss convergence of various DV-circuit QCPINN models with a classical PINN while solving the lid-driven cavity equation. The loss curves indicate that all DV-based models achieve stable convergence with minimal oscillations. Similar to Fig. 6, the angle embedding with the cascade topology circuit in Fig. 4 closely matches the loss level of the best classical model.

Fig. 7 visualizes the results obtained using the finite element method solution alongside the predicted solutions for the lid-driven cavity Eq. 5. It also shows the prediction errors for both the best classical model and the angle-cascade QCPINN. The classical PINN model and the angle-cascade QCPINN effectively capture the main flow features. The absolute error distributions (third and fifth rows) reveal distinct patterns in both velocity components and pressure fields. Both models exhibit higher errors near the top moving lid for velocity components, where the flow experiences the most significant shear.

6.2.3 Generalizing Our Solution.

Our experiments with the Helmholtz and lid-driven cavity problems, outlined in sections 6.2.1 and 6.2.2, revealed that the angle-cascade variant of the DV-circuit QCPINN architecture consistently outperforms other configurations. To validate the robustness of the angle-cascade QCPINN architecture across diverse physical systems, we expanded our evaluation to three additional canonical PDEs: the wave equation 6, the Klein-Gordon equation 7, and the convection-diffusion equation 8. This expansion allows us to assess whether the advantages of our quantum-enhanced architecture persist across problems with fundamentally different physical characteristics and computational challenges.

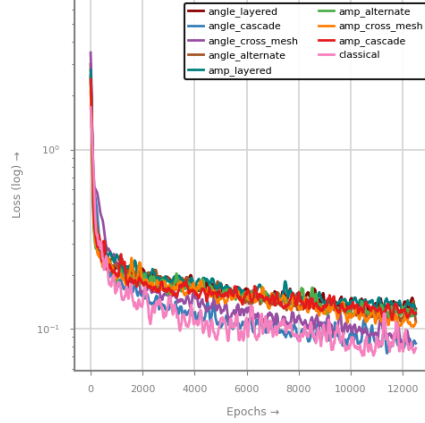


Figure 6: Training convergence history of our DV-based QCPINN models compared to the best classical PINN model (model-2) when solving the lid-driven cavity equation. The plots track the performance over 12500 epochs, showing how QCPINN performs with two different embedding methods across four circuit topologies.

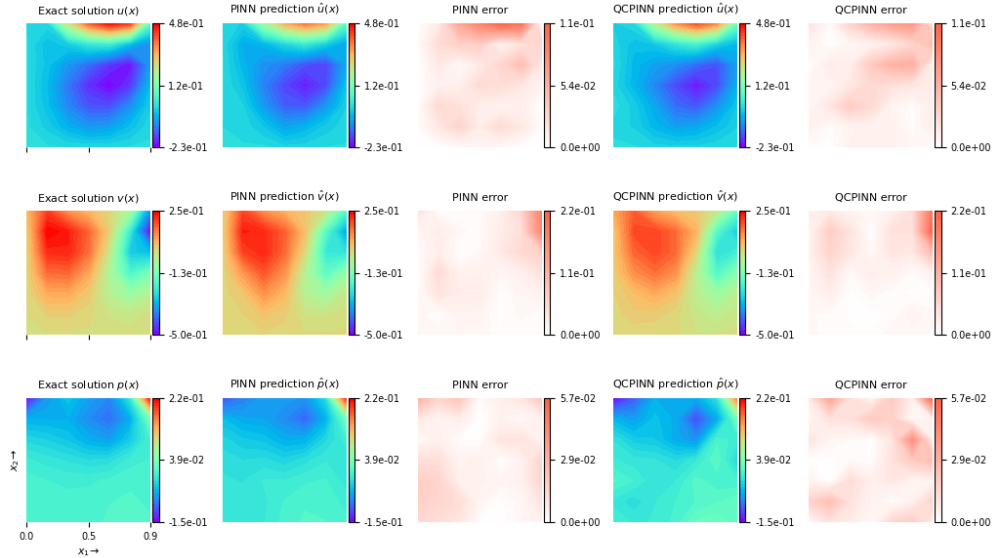


Figure 7: Comparison of the reference FEM solution and the model predictions for the lid-driven cavity equation: the classical PINN model-2 (which outperforms model-1), and our DV-circuit QCPINN using angle embedding (which outperforms amplitude embedding) with cascade topology (which outperforms the other three topologies). The first and second rows show the velocity fields (u and v), while the third row shows the pressure field (p).

Table 6 presents the performance of the angle-cascade DV-circuit QCPINN model for solving these three additional PDEs and comparing the results with the classical models. Our angle-cascade QCPINN model maintains its parameter efficiency advantage while achieving competitive or better accuracy compared to classical PINNs. For the wave equation, our model requires only a 9.8% parameters while achieving a 50.5% reduction in relative L_2 error. The Klein-Gordon equation presents additional complexity due to its coupled system nature. Although our model exhibits a slightly higher final training loss, it maintains comparable relative L_2 errors while using only 9.8% of the parameters required by model-1. Notably, for the convection-diffusion equation, angle-cascade QCPINN model with 821 parameters (compared to 7,901 in model-1) achieves a 43% reduction in relative L_2 error for the primary solution variable and demonstrates improved training convergence.

Fig. 8 compares the convergence behavior of the angle-cascade DV-circuit QCPINN model to the classical PINN model. For the wave equation, Fig. 8(a) shows that the angle-cascade QCPINN (blue line) demonstrates significantly faster initial convergence, achieving lower loss values within the first 5,000 epochs compared to the classical approach (pink

Table 6: Comparison of our DV-circuit QCPINN using angle embedding (which outperforms amplitude embedding) with cascade topology (which outperforms the other three topologies) with the two classical PINN models for solving wave, Klein-Gordon, and convection-diffusion equations. The comparison metrics include the number of trainable parameters required by each model, the relative L_2 error in %, and the final training loss value achieved. u and f are the reference solutions and the source term, respectively.

PDEs	Method	# Parameters	Relative L_2 error (%)		Final loss
wave Eq. 6	angle-cascade	771	u	$1.02e + 01$	0.083
	Classical PINN	7851	u	$2.06e + 01$	0.128
	model-2	2751	u	$8.68e + 00$	0.027
Klein-Gordon Eq. 7	angle-cascade	771	u	$1.17e + 01$	2.727
	Classical PINN	7851	f	$3.17e + 00$	
	model-2	2751	f	$3.35e + 00$	0.718
Convection-diffusion Eq. 8	angle-cascade	821	u	$1.20e + 01$	0.008
	Classical PINN	7901	u	$4.38e + 00$	
	model-2	2801	f	$3.11e + 00$	0.014
	model-2	2801	u	$2.06e + 01$	
	model-2	2801	f	$1.31e + 01$	0.1

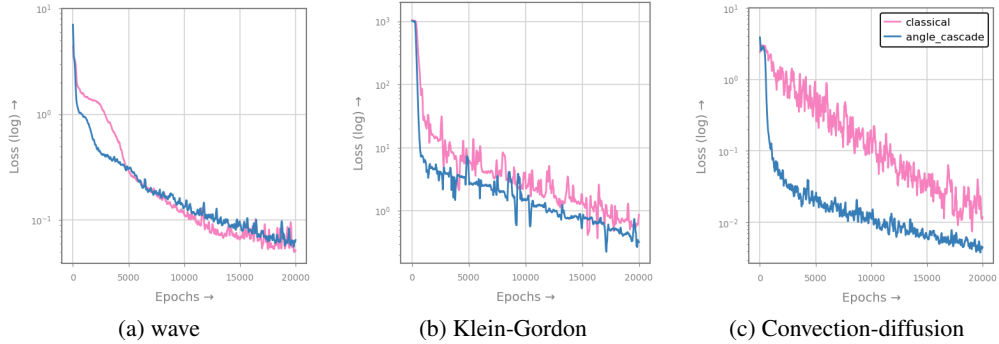


Figure 8: Training loss history for three PDEs: (a) wave, (b) Klein-Gordon, and (c) convection-diffusion. Each plot compares the convergence behavior of our angle-cascade QCPINN model (which outperforms the other embedding and topologies) against the best-performing classical PINN model (as reported in table 6) over 20,000 training epochs.

line). Likewise, for the Klein-Gordon equation, Fig. 8(b) shows that angle-cascade QCPINN maintains comparable convergence stability despite the equation’s coupled nature, with both models exhibiting similar loss trajectories after the initial training phase. Notably, for the convection-diffusion equation, Fig. 8(c) shows that our model consistently maintains a monotonic loss reduction throughout training, reaching a final loss approximately one order of magnitude lower than that of the classical approach.

Fig. 9 visualizes both reference and predicted solutions. For the wave equation, Fig. 9(a) shows that both the classical PINN and QCPINN capture the oscillatory pattern, but the error distribution of QCPINN (top-right plot) displays noticeably lower error magnitudes across the domain. The Klein-Gordon equation, Fig. 9(b), shows our model’s ability to accurately represent coupled solutions, with error distributions that are comparable to or better than those of the classical model. The convection-diffusion equation, Fig. 9(c), shows our model’s ability to precisely capture the sharp localized features characteristic of convection-dominated flows. The error visualization confirms significantly reduced prediction errors across solution components (u and f), with error magnitudes approximately 2 – 3 times lower than those of classical PINNs.

7 Conclusion

We found that QCPINN models achieve comparable solution accuracy to classical PINNs while requiring a fraction of trainable parameters – as little as 10% of those needed by their classical counterparts under about the same settings. The

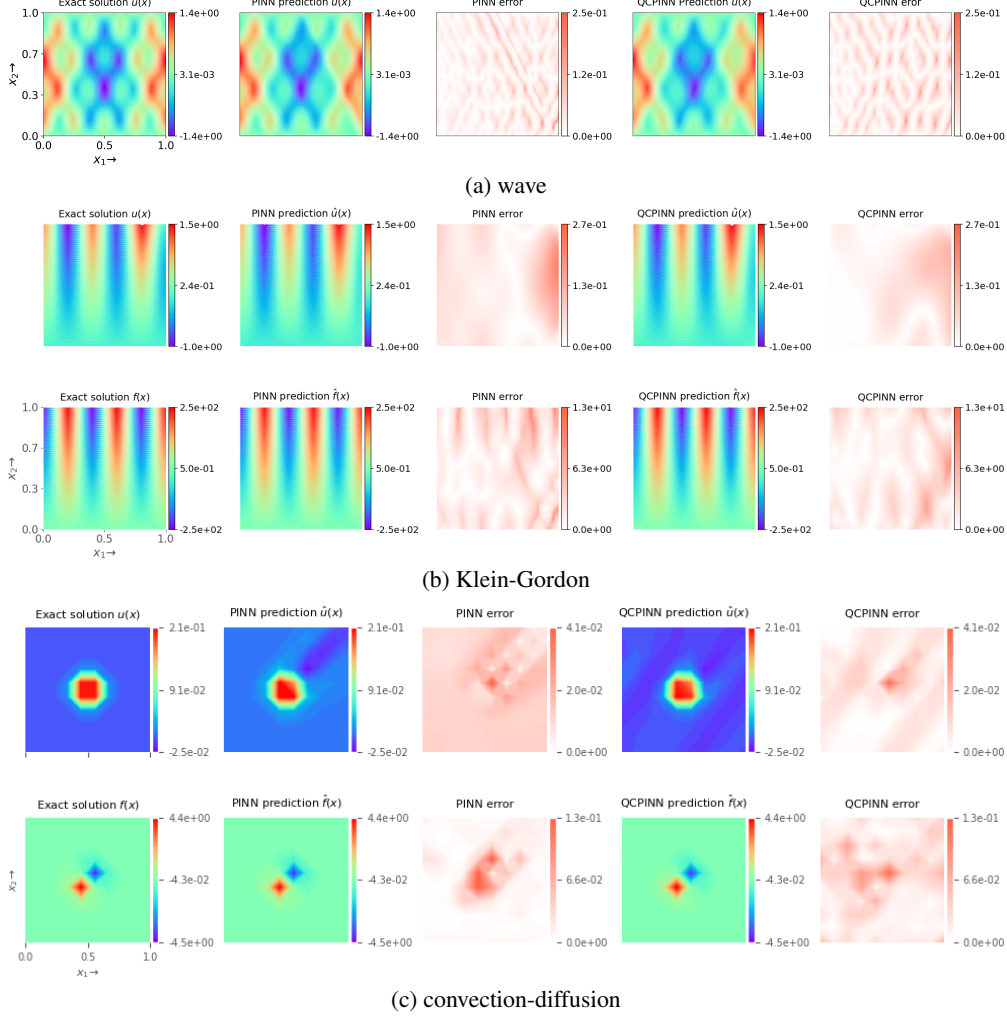


Figure 9: Comparison of the reference solution and the model predictions for three PDEs: (a) wave, (b) Klein-Gordon, and (c) convection-diffusion. For each equation, we present results from both the best-performing classical PINN model and angle-cascade DV-circuit QCPINN implementation. For each equation, the top row displays the velocity field (u), while the bottom row (if exists) shows the force field (f).

experimental evidence supports our hypothesis that hybrid quantum-classical approaches can maintain solution quality while dramatically improving parameter efficiency. Our systematic assessment of various QCPINN configurations across multiple PDEs consistently revealed that DV-circuit implementations with angle embedding and cascade topology offer the best performance. Notably, for the convection-diffusion equation, our angle-cascade QCPINN achieved around 40% reduction in relative L_2 error compared to classical models.

Our experimental results reveal that CV-circuits consistently show training instabilities and underperform compared to DV-circuits. Standard gradient-based optimization methods, like Adam, face significant challenges with CV-based quantum circuit models due to their sensitivity to parameter initialization and gradient dynamics. The vanishing gradient problem is worsened in CV circuits, where small initial parameter values are needed for stability, but these values also limit gradient magnitudes during backpropagation, creating a trade-off between stability and trainability.

The primary strength of this work lies in its comprehensive comparative study, which systematically evaluates two quantum circuit architectures: DV and CV, each assessed with various configurations. The CV circuits comprise two measurement schemes, three nonlinear operations, and two parameterization schemes, while the DV circuits consist of two embedding schemes and four circuit topologies, evaluated against two benchmark PDEs and generalizability against three additional benchmark PDEs. The open-source implementation further enhances reproducibility and enables community engagement. However, we acknowledge several limitations. While parameter efficiency was significantly

improved, overall solution accuracy remained comparable to classical PINNs rather than surpassing them, except for the convection-diffusion problem. Additionally, the highly non-convex PINN loss landscape still required careful weighting for the loss terms, which were determined through extensive empirical studies rather than exploring quantum circuit advantage to enhance this problem. Contrary to theoretical expectations, CV-circuit implementations exhibited training instabilities and underperformed relative to DV-circuit variants for the cases considered in this study.

Despite these limitations, our findings remain robust when examined through multiple performance metrics and across diverse PDE types. The consistent advantage of angle-cascade configurations in achieving lower relative L_2 errors and final training losses, combined with their significant parameter efficiency, represents a meaningful advancement in physics-informed machine learning.

Future research should explore more complex PDEs that require larger parameter spaces. By applying PINNs and QPINNs to these scenarios, a comparative analysis could highlight the benefits of QCPINNs and reveal advantages not evident in simpler domains or that PINNs cannot address. This broader investigation could enhance our understanding of when quantum-enhanced neural networks significantly improve solutions for complex PDEs. Additionally, studies should focus on advanced quantum circuit designs tailored to PDE characteristics and on developing optimization strategies to improve training stability, especially for CV-circuit quantum methods.

Acknowledgment

We thank the National Center for High-Performance Computing of Turkiye (UHeM) for providing computing resources under grant number 5010662021.

Keywords Quantum Computing · Neural networks · Physics-informed neural network · Partial differential equation · PINN · PDE

References

- [1] George Em Karniadakis, Ioannis G Kevrekidis, Lu Lu, Paris Perdikaris, Sifan Wang, and Liu Yang. Physics-informed machine learning. *Nature Reviews Physics*, 3(6):422–440, 2021.
- [2] Shengze Cai, Zhiping Mao, Zhicheng Wang, Minglang Yin, and George Em Karniadakis. Physics-informed neural networks (pinns) for fluid mechanics: A review. *Acta Mechanica Sinica*, 37(12):1727–1738, 2021.
- [3] Afrah Farea, Saiful Khan, Reza Daryani, Emre Cenk Ersan, and Mustafa Serdar Celebi. Learning fluid-structure interaction dynamics with physics-informed neural networks and immersed boundary methods. *arXiv preprint arXiv:2505.18565*, 2025.
- [4] Xue Ying. An overview of overfitting and its solutions. In *Journal of physics: Conference series*, volume 1168, page 022022. IOP Publishing, 2019.
- [5] Afrah Farea and Mustafa Serdar Celebi. Learnable activation functions in physics-informed neural networks for solving partial differential equations, 2025.
- [6] Kosuke Mitarai, Makoto Negoro, Masahiro Kitagawa, and Keisuke Fujii. Quantum circuit learning. *Physical Review A*, 98(3):032309, 2018.
- [7] Vojtěch Havlíček, Antonio D Cárcoles, Kristan Temme, Aram W Harrow, Abhinav Kandala, Jerry M Chow, and Jay M Gambetta. Supervised learning with quantum-enhanced feature spaces. *Nature*, 567(7747):209–212, 2019.
- [8] Marco Cerezo, Andrew Arrasmith, Ryan Babbush, Simon C Benjamin, Suguru Endo, Keisuke Fujii, Jarrod R McClean, Kosuke Mitarai, Xiao Yuan, Lukasz Cincio, et al. Variational quantum algorithms. *Nature Reviews Physics*, 3(9):625–644, 2021.
- [9] Maria Schuld, Ryan Sweke, and Johannes Jakob Meyer. Effect of data encoding on the expressive power of variational quantum-machine-learning models. *Physical Review A*, 103(3):032430, 2021.
- [10] Amira Abbas, David Sutter, Christa Zoufal, Aurélien Lucchi, Alessio Figalli, and Stefan Woerner. The power of quantum neural networks. *Nature Computational Science*, 1(6):403–409, 2021.
- [11] Yuxuan Du, Min-Hsiu Hsieh, Tongliang Liu, Shan You, and Dacheng Tao. Learnability of quantum neural networks. *PRX quantum*, 2(4):040337, 2021.
- [12] Alexandr Sedykh, Maninadh Podapaka, Asel Sagingalieva, Karan Pinto, Markus Pflitsch, and Alexey Melnikov. Hybrid quantum physics-informed neural networks for simulating computational fluid dynamics in complex shapes. *Machine Learning: Science and Technology*, 5(2):025045, 2024.

[13] Nahid Binandeh Dehaghani, A Pedro Aguiar, and Rafal Wisniewski. A hybrid quantum-classical physics-informed neural network architecture for solving quantum optimal control problems. In *2024 IEEE International Conference on Quantum Computing and Engineering (QCE)*, volume 1, pages 1378–1386. IEEE, 2024.

[14] Corey Trahan, Mark Loveland, and Samuel Dent. Quantum physics-informed neural networks. *Entropy*, 26(8):649, 2024.

[15] Fong Yew Leong, Wei-Bin Ewe, Tran Si Bui Quang, Zhongyuan Zhang, and Jun Yong Khoo. Hybrid quantum physics-informed neural network: Towards efficient learning of high-speed flows. *arXiv preprint arXiv:2503.02202*, 2025.

[16] Maziar Raissi, Paris Perdikaris, and George E Karniadakis. Physics-informed neural networks: A deep learning framework for solving forward and inverse problems involving nonlinear partial differential equations. *Journal of Computational Physics*, 378:686–707, 2019.

[17] Nathan Killoran, Thomas R Bromley, Juan Miguel Arrazola, Maria Schuld, Nicolás Quesada, and Seth Lloyd. Continuous-variable quantum neural networks. *Physical Review Research*, 1(3):033063, 2019.

[18] Jarrod R McClean, Sergio Boixo, Vadim N Smelyanskiy, Ryan Babbush, and Hartmut Neven. Barren plateaus in quantum neural network training landscapes. *Nature communications*, 9(1):4812, 2018.

[19] Marco Cerezo, Akira Sone, Tyler Volkoff, Lukasz Cincio, and Patrick J Coles. Cost function dependent barren plateaus in shallow parametrized quantum circuits. *Nature communications*, 12(1):1791, 2021.

[20] Zoë Holmes, Kunal Sharma, Marco Cerezo, and Patrick J Coles. Connecting ansatz expressibility to gradient magnitudes and barren plateaus. *PRX quantum*, 3(1):010313, 2022.

[21] Francesco Tacchino, Panagiotis Barkoutsos, Chiara Macchiavello, Ivano Tavernelli, Dario Gerace, and Daniele Bajoni. Quantum implementation of an artificial feed-forward neural network. *Quantum Science and Technology*, 5(4):044010, 2020.

[22] Stefano Mangini, Francesco Tacchino, Dario Gerace, Daniele Bajoni, and Chiara Macchiavello. Quantum computing models for artificial neural networks. *Europhysics Letters*, 134(1):10002, 2021.

[23] Aram W Harrow, Avinatan Hassidim, and Seth Lloyd. Quantum algorithm for linear systems of equations. *Physical review letters*, 103(15):150502, 2009.

[24] Andris Ambainis. Variable time amplitude amplification and quantum algorithms for linear algebra problems. In *STACS'12 (29th Symposium on Theoretical Aspects of Computer Science)*, volume 14, pages 636–647. LIPIcs, 2012.

[25] Rolando Somma, Andrew Childs, and Robin Kothari. Quantum linear systems algorithm with exponentially improved dependence on precision. In *APS March Meeting Abstracts*, volume 2016, pages H44–001, 2016.

[26] Sarah K Leyton and Tobias J Osborne. A quantum algorithm to solve nonlinear differential equations. *arXiv preprint arXiv:0812.4423*, 2008.

[27] Dominic W Berry. High-order quantum algorithm for solving linear differential equations. *Journal of Physics A: Mathematical and Theoretical*, 47(10):105301, 2014.

[28] Andrew M Childs and Jin-Peng Liu. Quantum spectral methods for differential equations. *Communications in Mathematical Physics*, 375(2):1427–1457, 2020.

[29] Dominic W Berry, Andrew M Childs, Aaron Ostrander, and Guoming Wang. Quantum algorithm for linear differential equations with exponentially improved dependence on precision. *Communications in Mathematical Physics*, 356:1057–1081, 2017.

[30] Jeffrey Yepez. Quantum lattice-gas model for the burgers equation. *Journal of Statistical Physics*, 107:203–224, 2002.

[31] Ashley Montanaro and Sam Pallister. Quantum algorithms and the finite element method. *Physical Review A*, 93(3):032324, 2016.

[32] Furkan Oz, Rohit KSS Vuppala, Kursat Kara, and Frank Gaitan. Solving burgers' equation with quantum computing. *Quantum Information Processing*, 21(1):30, 2022.

[33] Furkan Oz, Omer San, and Kursat Kara. An efficient quantum partial differential equation solver with chebyshev points. *Scientific Reports*, 13(1):7767, 2023.

[34] John Preskill. Reliable quantum computers. *Proceedings of the Royal Society of London. Series A: Mathematical, Physical and Engineering Sciences.*, 454(1969):385–410, 1998.

[35] Barbara M Terhal. Quantum error correction for quantum memories. *Reviews of Modern Physics*, 87(2):307–346, 2015.

[36] Andrew M Childs, Yuan Su, Minh C Tran, Nathan Wiebe, and Shuchen Zhu. Theory of trotter error with commutator scaling. *Physical Review X*, 11(1):011020, 2021.

[37] Sergey Bravyi and Alexei Kitaev. Universal quantum computation with ideal clifford gates and noisy ancillas. *Physical Review A—Atomic, Molecular, and Optical Physics*, 71(2):022316, 2005.

[38] Sergio Boixo, Sergei V Isakov, Vadim N Smelyanskiy, Ryan Babbush, Nan Ding, Zhang Jiang, Michael J Bremner, John M Martinis, and Hartmut Neven. Characterizing quantum supremacy in near-term devices. *Nature Physics*, 14(6):595–600, 2018.

[39] Scott Aaronson. Read the fine print. *Nature Physics*, 11(4):291–293, 2015.

[40] Carlo Ciliberto, Mark Herbster, Alessandro Davide Ialongo, Massimiliano Pontil, Andrea Rocchetto, Simone Severini, and Leonard Wossnig. Quantum machine learning: a classical perspective. *Proceedings of the Royal Society A: Mathematical, Physical and Engineering Sciences*, 474(2209):20170551, 2018.

[41] Seth Lloyd, Masoud Mohseni, and Patrick Rebentrost. Quantum algorithms for supervised and unsupervised machine learning. *arXiv preprint arXiv:1307.0411*, 2013.

[42] Maria Schuld and Nathan Killoran. Quantum machine learning in feature hilbert spaces. *Physical review letters*, 122(4):040504, 2019.

[43] Seth Lloyd, Maria Schuld, Aroosa Ijaz, Josh Izaac, and Nathan Killoran. Quantum embeddings for machine learning. *arXiv preprint arXiv:2001.03622*, 2020.

[44] Kerstin Beer, Dmytro Bondarenko, Terry Farrelly, Tobias J Osborne, Robert Salzmann, Daniel Scheiermann, and Ramona Wolf. Training deep quantum neural networks. *Nature communications*, 11(1):808, 2020.

[45] Adrián Pérez-Salinas, David López-Núñez, Artur García-Sáez, P. Forn-Díaz, and José I. Latorre. One qubit as a universal approximant. *Physical Review A*, 104:012405, Jul 2021.

[46] Takahiro Goto, Quoc Hoan Tran, and Kohei Nakajima. Universal approximation property of quantum machine learning models in quantum-enhanced feature spaces. *Physical Review Letters*, 127(9):090506, 2021.

[47] Yunchao Liu, Srinivasan Arunachalam, and Kristan Temme. A rigorous and robust quantum speed-up in supervised machine learning. *Nature Physics*, 17(9):1013–1017, 2021.

[48] Yudong Cao, Jonathan Romero, Jonathan P Olson, Matthias Degroote, Peter D Johnson, Mária Kieferová, Ian D Kivlichan, Tim Menke, Borja Peropadre, Nicolas PD Sawaya, et al. Quantum chemistry in the age of quantum computing. *Chemical reviews*, 119(19):10856–10915, 2019.

[49] Bela Bauer, Sergey Bravyi, Mario Motta, and Garnet Kin-Lic Chan. Quantum algorithms for quantum chemistry and quantum materials science. *Chemical Reviews*, 120(22):12685–12717, 2020.

[50] Benjamin Nachman, Davide Provasoli, Wibe A De Jong, and Christian W Bauer. Quantum algorithm for high energy physics simulations. *Physical review letters*, 126(6):062001, 2021.

[51] Carlo A Trugenberger. Quantum pattern recognition. *Quantum Information Processing*, 1:471–493, 2002.

[52] Alberto Peruzzo, Jarrod McClean, Peter Shadbolt, Man-Hong Yung, Xiao-Qi Zhou, Peter J Love, Alán Aspuru-Guzik, and Jeremy L O’brien. A variational eigenvalue solver on a photonic quantum processor. *Nature communications*, 5(1):4213, 2014.

[53] Jarrod R McClean, Jonathan Romero, Ryan Babbush, and Alán Aspuru-Guzik. The theory of variational hybrid quantum-classical algorithms. *New Journal of Physics*, 18(2):023023, 2016.

[54] Carlos Bravo-Prieto, Ryan LaRose, Marco Cerezo, Yigit Subasi, Lukasz Cincio, and Patrick J Coles. Variational quantum linear solver. *Quantum*, 7:1188, 2023.

[55] Anton Simen Albino, Lucas Correia Jardim, Diego Campos Knupp, Antonio Jose Silva Neto, Otto Menegasso Pires, and Erick Giovani Sperandio Nascimento. Solving partial differential equations on near-term quantum computers. *arXiv preprint arXiv:2208.05805*, 2022.

[56] Oleksandr Kyriienko, Annie E Paine, and Vincent E Elfving. Solving nonlinear differential equations with differentiable quantum circuits. *Physical Review A*, 103(5):052416, 2021.

[57] Daniel Bultrini and Oriol Vendrell. Mixed quantum-classical dynamics for near term quantum computers. *Communications Physics*, 6(1):328, 2023.

[58] Annie E Paine, Vincent E Elfving, and Oleksandr Kyriienko. Quantum kernel methods for solving regression problems and differential equations. *Physical Review A*, 107(3):032428, 2023.

[59] Michael Lubasch, Jaewoo Joo, Pierre Moinier, Martin Kiffner, and Dieter Jaksch. Variational quantum algorithms for nonlinear problems. *Physical Review A*, 101(1):010301, 2020.

[60] Samuel L Braunstein and Peter Van Loock. Quantum information with continuous variables. *Reviews of modern physics*, 77(2):513–577, 2005.

[61] Stefano Markidis. On physics-informed neural networks for quantum computers. *Frontiers in Applied Mathematics and Statistics*, 8:1036711, 2022.

[62] Abhishek Setty, Rasul Abdusalamov, and Felix Motzoi. Self-adaptive physics-informed quantum machine learning for solving differential equations. *Machine Learning: Science and Technology*, 6(1):015002, 2025.

[63] John Preskill. Quantum computing in the nisq era and beyond. *Quantum*, 2:79, 2018.

[64] Kishor Bharti, Alba Cervera-Lierta, Thi Ha Kyaw, Tobias Haug, Sumner Alperin-Lea, Abhinav Anand, Matthias Degroote, Hermanni Heimonen, Jakob S Kottmann, Tim Menke, et al. Noisy intermediate-scale quantum algorithms. *Reviews of Modern Physics*, 94(1):015004, 2022.

[65] Aditi Krishnapriyan, Amir Gholami, Shandian Zhe, Robert Kirby, and Michael W Mahoney. Characterizing possible failure modes in physics-informed neural networks. *Advances in neural information processing systems*, 34:26548–26560, 2021.

[66] Sifan Wang, Shyam Sankaran, Hanwen Wang, Yue Yu, Andrew Paris, and Paris Perdikaris. Approximation analysis of physics-informed neural networks under the neural tangent kernel framework. *Neural Networks*, 153:123–140, 2022.

[67] Yeonjong Shin, Zhongqiang Zhang, and George Em Karniadakis. Error estimates of residual minimization using neural networks for linear pdes. *Journal of Machine Learning for Modeling and Computing*, 4(4), 2023.

[68] Ville Bergholm, Josh Izaac, Maria Schuld, Christian Gogolin, Shahnawaz Ahmed, Vishnu Ajith, M Sohaib Alam, Guillermo Alonso-Linaje, B AkashNarayanan, Ali Asadi, et al. PennyLane: Automatic differentiation of hybrid quantum-classical computations. *arXiv preprint arXiv:1811.04968*, 2018.

[69] Michael Broughton, Guillaume Verdon, Trevor McCourt, Antonio J Martinez, Jae Hyeon Yoo, Sergei V Isakov, Philip Massey, Ramin Halavati, Murphy Yuezhen Niu, Alexander Zlokapa, et al. Tensorflow quantum: A software framework for quantum machine learning. *arXiv preprint arXiv:2003.02989*, 2020.

[70] Zongyi Li, Nikola Kovachki, Kamyar Azizzadenesheli, Burigede Liu, Kaushik Bhattacharya, Andrew Stuart, and Anima Anandkumar. Fourier neural operator for parametric partial differential equations. *arXiv preprint arXiv:2010.08895*, 2020.

[71] Edward Farhi and Hartmut Neven. Classification with quantum neural networks on near term processors. *arXiv preprint arXiv:1802.06002*, 2018.

[72] Sukin Sim, Peter D Johnson, and Alán Aspuru-Guzik. Expressibility and entangling capability of parameterized quantum circuits for hybrid quantum-classical algorithms. *Advanced Quantum Technologies*, 2(12):1900070, 2019.

[73] Ben Jaderberg, Abhishek Agarwal, Karsten Leonhardt, Martin Kiffner, and Dieter Jaksch. Minimum hardware requirements for hybrid quantum-classical dmft. *Quantum Science and Technology*, 5(3):034015, 2020.

[74] Lukas Mouton, Florentin Reiter, Ying Chen, and Patrick Rebentrost. Deep-learning-based quantum algorithms for solving nonlinear partial differential equations. *Physical Review A*, 110(2):022612, 2024.

[75] Nathan Killoran, Josh Izaac, Nicolás Quesada, Ville Bergholm, Matthew Amy, and Christian Weedbrook. Strawberry fields: A software platform for photonic quantum computing. *Quantum*, 3:129, 2019.

[76] Alexander I Lvovsky. Squeezed light. *Photonics: Scientific Foundations, Technology and Applications*, 1:121–163, 2015.

[77] A Ferraro, S Olivares, and MGA Paris. Gaussian states in quantum information (bibliopolis, napolì, 2005). *Dell'Anno et al., Phys. Rep.*, 428:53, 2006.

[78] PD Drummond and DF Walls. Quantum theory of optical bistability. i. nonlinear polarisability model. *Journal of Physics A: Mathematical and General*, 13(2):725, 1980.

[79] Xavier Glorot and Yoshua Bengio. Understanding the difficulty of training deep feedforward neural networks. In *Proceedings of the thirteenth international conference on artificial intelligence and statistics*, pages 249–256. JMLR Workshop and Conference Proceedings, 2010.

A PDEs

A.1 Helmholtz Equation

The Helmholtz equation represents a fundamental PDE in mathematical physics, arising as the time-independent form of the wave equation. We consider a two-dimensional Helmholtz equation of the form:

$$\begin{aligned}\Delta u(x, y) + k^2 u(x, y) &= f(x, y) & (x, y) \in \Omega \\ u(x, y) &= h(x, y) & (x, y) \in \Gamma_0\end{aligned}\quad (4)$$

where Δ is the Laplacian operator defined as $\Delta u = \frac{\partial^2 u}{\partial x^2} + \frac{\partial^2 u}{\partial y^2}$, k is the wavenumber (related to the frequency of oscillation), $f(x, y)$ is the forcing term (source function), $h(x, y)$ specifies the Dirichlet boundary conditions. In this study, we choose an exact solution of the form:

$$u(x, y) = \sin(a_1 \pi x) \sin(a_2 \pi y)$$

on the square domain $\Omega = [-1, 1] \times [-1, 1]$ with Wavenumber $k = 1$, first mode number $a_1 = 1$, and the second mode number $a_2 = 4$. This choice of solution leads to a corresponding source term:

$$f(x, y) = u(x, y)[k^2 - (a_1 \pi)^2 - (a_2 \pi)^2]$$

To solve this problem using QCPINN, we construct a loss function that incorporates both the physical governing equation and the boundary conditions:

$$\begin{aligned}\mathcal{L}(\theta) &= \min_{\theta} (\lambda_1 \|\mathcal{L}_{\text{phy}}(\theta)\|_{\Omega} + \lambda_2 \|\mathcal{L}_{\text{bc}}(\theta)\|_{\Gamma_0}) \\ &= \min_{\theta} (\lambda_1 \text{MSE}(\underbrace{\|u_{\theta_{xx}}(x, y) + u_{\theta_{yy}}(x, y) + \alpha u_{\theta}(x, y)\|_{\Omega}}_{\text{PDE residual}}) + \text{MSE}(\lambda_2 \underbrace{\|u_{\theta}(x, y) - u(x, y)\|_{\Gamma_0}}_{\text{Boundary condition}}))\end{aligned}$$

where $\alpha = (a_1 \pi)^2 + (a_2 \pi)^2$ combines the mode numbers into a single parameter. The chosen loss weights are $\lambda_1 = 1.0$ and $\lambda_2 = 10.0$.

A.2 Time-dependent 2D lid-driven cavity Problem

The lid-driven cavity flow is a classical CFD benchmark problem that is a fundamental test case for many numerical methods where flow is governed by the unsteady, incompressible Navier-Stokes equations. The momentum equation, continuity equation, initial condition, no-slip boundary on walls, and moving lid condition are defined, respectively, as :

$$\begin{aligned}\rho \left(\frac{\partial \mathbf{u}}{\partial t} + \mathbf{u} \cdot \nabla \mathbf{u} \right) &= -\nabla p + \mu \nabla^2 \mathbf{u} \\ \nabla \cdot \mathbf{u} &= 0 \\ \mathbf{u}(0, \mathbf{x}) &= 0 \\ \mathbf{u}(t, \mathbf{x}_0) &= 0 \quad \mathbf{x} \in \Gamma_0 \\ \mathbf{u}(t, \mathbf{x}_l) &= 1 \quad \mathbf{x} \in \Gamma_1\end{aligned}\quad (5)$$

The computational domain is $\Omega = (0, 1) \times (0, 1)$, the spatial discretization, $(N_x, N_y) = (100, 100)$ is uniform grid, with temporal domain $t \in [0, 10]$ seconds and $\Delta t = 0.01$ s with density $\rho = 1056 \text{ kg/m}^3$, viscosity $\mu = 1/\text{Re} = 0.01 \text{ kg/(m}\cdot\text{s)}$, where Re is the Reynolds number. Γ_1 is the top boundary (moving lid) with tangential velocity $U = 1 \text{ m/s}$, and Γ_0 is the remaining three sides with no-slip condition ($\mathbf{u} = 0$) where $\mathbf{u} = (u, v)$.

For validation purposes, we compare the neural network approximation with results obtained using the finite volume method. The PINN approach employs a composite loss function:

$$\mathcal{L}(\theta) = \min_{\theta} \left[\lambda_1 \underbrace{\|\mathcal{L}_{\text{phy}}(\theta)\|_{\Omega}}_{\text{PDE residual}} + \lambda_2 \underbrace{\|\mathcal{L}_{\text{up}}(\theta) + \mathcal{L}_{\text{bc}_1}(\theta)\|_{\Gamma_1 \cup \Gamma_0}}_{\text{Boundary conditions}} + \lambda_3 \underbrace{\|\mathcal{L}_{\text{u0}}(\theta)\|_{\Omega}}_{\text{Initial conditions}} \right]$$

where, the physics-informed loss component, $\mathcal{L}_{\text{phy}}(\theta)$ consists of three terms:

$$\mathcal{L}_{\text{phy}}(\theta) = \mathcal{L}_{r_u} + \mathcal{L}_{r_v} + \mathcal{L}_{r_c}$$

such that,

$$\begin{aligned}\mathcal{L}_{r_u}(\theta) &= \text{MSE} \left[(u_{\theta_t} + u_{\theta}u_{\theta_x} + v_{\theta}u_{\theta_y}) + \frac{1.0}{\rho}p_{\theta_x} - \mu(u_{\theta_{xx}} + u_{\theta_{yy}}) \right] \\ \mathcal{L}_{r_v}(\theta) &= \text{MSE} \left[(v_{\theta_t} + u_{\theta}v_{\theta_x} + v_{\theta}v_{\theta_y}) + \frac{1.0}{\rho}p_{\theta_y} - \mu(v_{\theta_{xx}} + v_{\theta_{yy}}) \right] \\ \mathcal{L}_{r_c}(\theta) &= \text{MSE} [u_{\theta_x} + v_{\theta_y}]\end{aligned}$$

The boundary and initial conditions are enforced through the following:

$$\begin{aligned}\mathcal{L}_{\text{up}} &= \text{MSE} [(1.0 - \hat{u}) + \hat{v}] \\ \mathcal{L}_{\text{bc}_1} &= \mathcal{L}_{\text{bottom, right, left}} = \text{MSE} [\hat{u} + \hat{v}] \\ \mathcal{L}_{\text{u0}} &= \text{MSE} [\hat{u} + \hat{v} + \hat{p}]\end{aligned}$$

where, \mathcal{L}_{up} is the moving lid, $\mathcal{L}_{\text{bc}_1}$ is the no-slip walls, \mathcal{L}_{u0} is the initial conditions. The loss weights are empirically chosen as $\lambda_1 = 0.1$, $\lambda_2 = 2.0$, $\lambda_3 = 4.0$ for \mathcal{L}_{phy} , \mathcal{L}_{up} , $\mathcal{L}_{\text{bc}_1}$ and \mathcal{L}_{u0} respectively.

A.3 1D Wave Equation

The wave equation is a fundamental second-order hyperbolic partial differential equation that models various physical phenomena. In its one-dimensional form, it describes the evolution of a disturbance along a single spatial dimension over time. The general form of the time-dependent 1D wave equation is:

$$\begin{aligned}u_{tt}(t, x) - c^2 u_{xx}(t, x) &= 0 & (t, x) \in & \\ u(t, x_0) = f_1(t, x) & & (t, x) \text{ on } & \Gamma_0 \\ u(t, x_1) = f_2(t, x) & & (t, x) \text{ on } & \Gamma_1 \\ u(0, x) = g(t, x) & & (t, x) \in & \Omega \\ u_t(0, x) = h(t, x) & & (t, x) \in & \partial\Omega\end{aligned} \tag{6}$$

where $u(t, x)$ represents the wave amplitude at position x and time t , and c is the wave speed characterizing the medium's properties. The subscripts denote partial derivatives: u_{tt} is the second time derivative, and u_{xx} is the second spatial derivative.

For our numerical investigation, we consider a specific case with the following parameters: $c = 2$, $a = 0.5$, $f_1 = f_2 = 0$. The exact solution is chosen as:

$$u(t, x) = \sin(\pi x) \cos(c\pi t) + 0.5 \sin(2c\pi x) \cos(4c\pi t)$$

This solution represents a superposition of two standing waves with different spatial and temporal frequencies. The problem is defined on the unit square domain $(t, x) \in [0, 1] \times [0, 1]$, leading to the specific boundary value problem:

$$\begin{aligned}u_{tt}(t, x) - 4u_{xx}(t, x) &= 0 & (t, x) \in \Omega = [0, 1] \times [0, 1] \\ u(t, 0) = u(t, 1) &= 0 \\ u(0, x) &= \sin(\pi x) + 0.5 \sin(4\pi x) & x \in [0, 1] \\ u_t(0, x) &= 0\end{aligned}$$

To solve this problem using the proposed hybrid QCPINN, we construct a loss function that incorporates the physical constraints, boundary conditions, and initial conditions:

$$\begin{aligned}
\mathcal{L}(\theta) &= \min_{\theta} [\lambda_1 \|\mathcal{L}_{\text{phy}}(\theta)\|_{\Omega} + \lambda_2 \|\mathcal{L}_{\text{bc}}(\theta)\|_{\Gamma_1} + \lambda_3 \|\mathcal{L}_{\text{ic}}(\theta)\|_{\Gamma_0}] \\
&= \min_{\theta} [\lambda_1 \text{MSE}(\underbrace{\|u_{\theta_{tt}}(t, x) - 4u_{\theta_{xx}}(t, x)\|_{\Omega}}_{\text{PDE residual}}) \\
&\quad + \lambda_2 \text{MSE}(\underbrace{\|u_{\theta}(t, 0) + u_{\theta}(t, 1) + u_{\theta}(0, x) - \sin(\pi x) - 0.5 \sin(4\pi x)\|_{\Gamma_0 \cap \Gamma_1}}_{\text{Boundary/initial conditions}}) \\
&\quad + \lambda_3 \text{MSE}(\underbrace{\|u_{\theta_t}(0, x)\|_{\partial\Omega}}_{\text{Initial velocity}})]
\end{aligned}$$

The loss weights are empirically chosen as $\lambda_1 = 0.1$, $\lambda_2 = 10.0$ and $\lambda_3 = 0.1$.

A.4 Klein-Gordon Equation

The Klein-Gordon equation is a significant second-order hyperbolic PDE that emerges in numerous theoretical physics and applied mathematics areas. The equation represents a natural relativistic extension of the Schrödinger equation. In this study, we consider the one-dimensional nonlinear Klein-Gordon equation of the form:

$$\begin{aligned}
u_{tt} - \alpha u_{xx} + \beta u + \gamma u^k &= 0 \quad (t, x) \in \Omega \\
u(t, x) &= g_1(t, x) \quad (t, x) \text{ on } \Gamma_0 \\
u_t(t, x) &= g_2(t, x) \quad (t, x) \text{ on } \Gamma_1 \\
u(0, x) &= h(t, x) \quad (t, x) \in \partial\Omega \times [0, T]
\end{aligned} \tag{7}$$

where α is the wave speed coefficient, β is the linear term coefficient, γ is the nonlinear term coefficient, and k is the nonlinearity power. For our numerical study, we set $\alpha = 1$, $\beta = 0$, $\gamma = 1$ and $k = 3$. We choose an exact solution of the form:

$$u(t, x) = x \cos(5\pi t) + (tx)^3$$

This solution combines oscillatory behavior with polynomial growth, providing a challenging test case for our numerical method. The complete boundary value problem on the unit square domain becomes:

$$\begin{aligned}
u_{tt}(t, x) - u_{xx}(t, x) + u^3(t, x) &= 0 \quad (t, x) \in \Omega = [0, 1] \times [0, 1] \\
u(t, 0) &= 0 \\
u(t, 1) &= \cos(5\pi t) + t^3 \\
u(0, x) &= x \\
u_t(0, x) &= 0
\end{aligned}$$

To solve this nonlinear PDE using the proposed QCPINN, we construct a composite loss function incorporating the physical constraints, boundary conditions, and initial conditions:

$$\begin{aligned}
\mathcal{L}(\theta) &= \min_{\theta} [\lambda_1 \|\mathcal{L}_{\text{phy}}(\theta)\|_{\Omega} + \lambda_2 \|\mathcal{L}_{\text{bc}}(\theta)\|_{\Gamma_1} + \lambda_3 \|\mathcal{L}_{\text{ic}}(\theta)\|_{\Gamma_0}] \\
&= \min_{\theta} [\lambda_1 \text{MSE}(\underbrace{\|u_{\theta_{tt}}(t, x) - u_{\theta_{xx}}(t, x) + u^3(t, x)\|_{\Omega}}_{\text{PDE residual}}) \\
&\quad + \lambda_2 \text{MSE}(\underbrace{\|u(t, 0) + u(t, 1) - \cos(5\pi t) + t^3 + u(0, x) - x\|_{\Gamma_1}}_{\text{Boundary/initial conditions}}) \\
&\quad + \lambda_3 \text{MSE}(\underbrace{\|u_{\theta_t}(0, x)\|_{\partial\Omega}}_{\text{Initial velocity}})]
\end{aligned}$$

The loss weights are chosen empirically to balance the different components as $\lambda_1 = 1.0$, $\lambda_2 = 10.0$, and $\lambda_3 = 1.0$.

A.5 Convection-diffusion Equation

The problem focuses on solving the 2D convection-diffusion equation, a partial differential equation that models the transport of a quantity under convection (bulk movement) and diffusion (spreading due to gradients). The specific form considered here includes a viscous 2D convection-diffusion equation of the form:

$$\begin{aligned} u_t + c_1 u_x + c_2 u_y - D \Delta u(x, y) &= 0 & (t, x, y) \in \Omega \\ u(t, \mathbf{x}) &= g_0(t, \mathbf{x}) & (t, \mathbf{x}) \in \Gamma_0 \\ u(t, \mathbf{x}) &= g_1(t, \mathbf{x}) & (t, \mathbf{x}) \in \Gamma_1 \\ u(0, \mathbf{x}) &= h(0, \mathbf{x}) & \mathbf{x} \in \partial\Omega \times [0, T] \end{aligned} \tag{8}$$

where c_1 is the convection velocity in the x direction, c_2 is the convection velocity in the y direction, D is the diffusion coefficient, and $\Delta = \frac{\partial^2}{\partial x^2} + \frac{\partial^2}{\partial y^2}$ is the Laplacian operator. For our numerical investigation, we choose an exact solution describing a Gaussian pulse:

$$u(t, x, y) = \exp(-100((x - 0.5)^2 + (y - 0.5)^2)) \exp(-t)$$

The corresponding initial condition is:

$$h(0, x, y) = \exp(-100((x - 0.5)^2 + (y - 0.5)^2))$$

We choose $c_1 = 1.0$, $c_2 = 1.0$, and $D = 0.01$. The complete initial-boundary value problem on the unit cube domain becomes:

$$\begin{aligned} u_t(t, x, y) + u_x(t, x, y) + u_y(t, x, y) - 0.01(u_{xx}(t, x, y) + u_{yy}(t, x, y)) &= 0 \\ u(t, x, y) &= g(t, x, y) \\ u(0, x, y) &= h(x, y) \end{aligned}$$

where $(t, x, y) \in \Omega = [0, 1] \times [0, 1] \times [0, 1]$. To solve this problem using the proposed QCPINN model, we formulate a loss function that incorporates the physical governing equation, boundary conditions, and initial conditions:

$$\begin{aligned} \mathcal{L}(\theta) &= \min_{\theta} (\lambda_1 \|\mathcal{L}_{\text{phy}}(\theta)\|_{\Omega} + \lambda_2 \|\mathcal{L}_{\text{bc}}(\theta)\|_{\Gamma_1} + \lambda_3 \|\mathcal{L}_{\text{ic}}(\theta)\|_{\Gamma_0}) \\ &= \min_{\theta} \left[\lambda_1 \underbrace{\min(\|u_{\theta_t}(t, x, y) + u_{\theta_x}(t, x, y) + u_{\theta_y}(t, x, y) - 0.01(u_{\theta_{xx}}(t, x, y) + u_{\theta_{yy}}(t, x, y))\|_{\Omega}}_{\text{PDE residual}} \right. \\ &\quad \left. + \lambda_2 \min(\|u(t, x, y) - g_1(t, x, y)\|_{\Gamma_1}) + \lambda_3 \min(\|u_{\theta}(0, x, y) - h(x, y)\|_{\Omega_0}) \right] \end{aligned}$$

The loss weights are chosen to balance the different components $\lambda_1 = 1.0$, $\lambda_2 = 10.0$, and $\lambda_3 = 10.0$.